Available online at www.sciencedirect.com
SCIENCE DIRECT®
Nuclear Physics A 735 (2004) 303–328
NUCLEAR PHYSICS A
www.elsevier.com/locate/npe

Reaction cross section and matter radius measurements of proton-rich Ga, Ge, As, Se and Br nuclides

G.F. Lima [a,b], A. Lépine-Szily [a,*], A.C.C. Villari [c], W. Mittig [c], R. Lichtenthäler [a], M. Chartier [c,d], N.A. Orr [e], J.C. Angélique [e], G. Audi [f], E. Baldini-Neto [g], B.V. Carlson [g], J.M. Casandjian [c], A. Cunsolo [h], C. Donzaud [i], A. Foti [h], A. Gillibert [j], D. Hirata [k], M. Lewitowicz [c], S. Lukyanov [l], M. MacCormick [i], D.J. Morrissey [m], A.N. Ostrowski [c,n], B.M. Sherrill [m], C. Stephan [i], T. Suomijärvi [i,m], L. Tassan-Got [i], D.J. Vieira [o], J.M. Wouters [o]

[a] *Instituto de Física, Universidade de São Paulo, C.P. 66318, 05315-970 São Paulo, Brazil*
[b] *FACENS—Faculdade de Engenharia de Sorocaba, C.P. 355, 18001-970 Sorocaba, SP, Brazil*
[c] *GANIL, Boulevard Henry Becquerel, BP 5027, 14021 Caen cedex, France*
[d] *University of Liverpool, Department of Physics, Liverpool, L69 7ZE, UK*
[e] *LPC, IN2P3-CNRS, ISMRA et Université de Caen, 14050 Caen cedex, France*
[f] *CSNSM (IN2P3-CNRS&UPS), Bâtiment 108, 91405 Orsay Campus, France*
[g] *Departamento de Física, Instituto Tecnológico de Aeronáutica, 12228-900 São José dos Campos, Brazil*
[h] *INFN, Corso Itália 57, 95129 Catania, Italy*
[i] *IPN Orsay, BP1, 91406 Orsay cedex, France*
[j] *CEA/DSM/DAPNIA/SPhN, CEN Saclay, 91191 Gif-sur-Yvette, France*
[k] *Department of Physics and Astronomy, The Open University, Milton Keynes, MK7 6AA, UK*
[l] *LNR, JINR, Dubna, P.O. Box 79, 101000 Moscow, Russia*
[m] *NSCL, Michigan State University, East Lansing, MI 48824-1321, USA*
[n] *Department of Physics and Astronomy, University of Edinburgh, Edinburgh, EH9 3JZ, UK*
[o] *Los Alamos National Laboratory, Los Alamos, NM 87545, USA*

Received 16 October 2003; received in revised form 5 January 2004; accepted 20 January 2004

Abstract

Proton-rich isotopes of Ga, Ge, As, Se and Br had their total reaction cross sections (σ_R) measured. Root-mean-squared matter radii were determined from Glauber model calculations, which

* Corresponding author.
E-mail address: alinka.lepine@dfn.if.usp.br (A. Lépine-Szily).

0375-9474/$ – see front matter
doi:10.1016/j.nuclphysa.2004.01.125

reproduced the experimental σ_R values. For all isotopic series a decrease of the $r_{\rm rms}$ with increasing neutron number was observed.

PACS: 21.10.Gv; 25.60.Dz; 27.50.+e

Keywords: NUCLEAR REACTIONS Si(^{63}Ga, X), (^{64}Ga, X), (^{65}Ga, X), (^{66}Ga, X), (^{67}Ga, X), (^{68}Ga, X), (^{65}Ge, X), (^{66}Ge, X), (^{67}Ge, X), (^{68}Ge, X), (^{69}Ge, X), (^{70}Ge, X), (^{67}As, X), (^{68}As, X), (^{69}As, X), (^{70}As, X), (^{71}As, X), (^{72}As, X), (^{69}Se, X), (^{70}Se, X), (^{71}Se, X), (^{72}Se, X), (^{73}Se, X), (^{72}Br, X), (^{73}Br, X), (^{74}Br, X), (^{75}Br, X), $E \sim 50$–60 MeV/nucleon; measured reaction σ. ^{63,64,65,66,67,68}Ga, ^{65,66,67,68,69,70}Ge, ^{67,68,69,70,71,72}As, ^{69,70,71,72,73}Se, ^{72,73,74,75}Br; deduced matter radii. Glauber model analysis

1. Introduction

One of the most exciting recent results in nuclear physics was the discovery of extended neutron distributions in light, neutron-rich nuclei, as, e.g., ^{11}Li and ^{11}Be, also called neutron halo [1]. The existence of the halo is a result of the barrier penetration of weakly bound, mainly s- or p-state ($l = 0$ or 1) valence neutron or pair of neutrons. The advent of facilities that produce radioactive ion beams made possible to search for experimental evidences of neutron halos or neutron skins. This phenomenon was first observed in the interaction radii obtained from reaction cross section measurements by Tanihata and collaborators [2] followed by the measurement of the transverse momentum distributions of break-up products of the halo nuclei [3].

Very precise methods, as laser-spectroscopy, were used to study the evolution with isotopic and isospin numbers of the charge radii of many unstable nuclei [4]. However other methods have to be used for the determination of the matter radii of unstable nuclei. The interaction cross-sections of many light, neutron-rich nuclei of the p and s–d shell were measured and the effective root-mean-squared matter radii could be deduced in recent studies. The evidence of neutron skin, excess of neutrons at the nuclear surface, was found for ^{6,8}He [5,6] and for ^{20}N. The existence of neutron skin increasing with isospin was shown by Suzuki and collaborators for the Na isotopic chain [7]. A recent paper reviews the main topics of nuclear sizes and gives experimental and theoretical references on the subject [8].

Proton halos are expected to be less pronounced due to the Coulomb barrier. Proton halo was first observed for the ^{8}B proton drip-line nucleus, deduced from the narrow width of the longitudinal momentum distribution of ^{7}Be fragments from the ^{8}B break-up reactions on light and heavy targets [9–12]. The tail of the $l = 1$ odd proton orbital in ^{8}B has an important role in the proton capture reaction on ^{7}Be, with contribution to the solar neutrino problem [13,14]. Recent measurements [15] indicate proton halos in the ground state of ^{26,27,28}P, where the valence proton in the ground-state has orbital angular momentum $l = 0$. Recent studies [16] indicate that the ground state of the ^{17}Ne nucleus is a two proton halo state. Proton skin was observed in recent days in the ^{31}Ar isotope, and the proton skin thickness increases monotonically with decreasing neutron number for the Ar isotopic chain [17].

In this paper we report on the first measurements of root-mean-squared matter radii of proton-rich isotopes of Ga, Ge, As, Se and Br, involved in the rp-process of explosive nucleosynthesis. The question is whether any of these proton-rich isotopes present anomalies in the radius. The radii were obtained from the reaction cross-sections σ_R measured at intermediate energies (50–60 A MeV), where the reaction cross-section is higher and thus more sensitive to surface phenomena as skin or halo.

2. Experimental method

The radioactive ions were produced at the Grand Accélérateur National d'Ions Lourds (GANIL), Caen, France, through the fragmentation of a 73 A MeV primary beam of ^{78}Kr, hitting a 90 mg/cm^2 thick ^{nat}Ni target, located between the two superconductor solenoids of the SISSI device [18]. Details of the experiment were described in recent papers [19,20]. The experimental setup is shown on the left panel of Fig. 1. After the selection of the reaction products [19,21] by the α-shaped spectrometer, they were driven to the high-

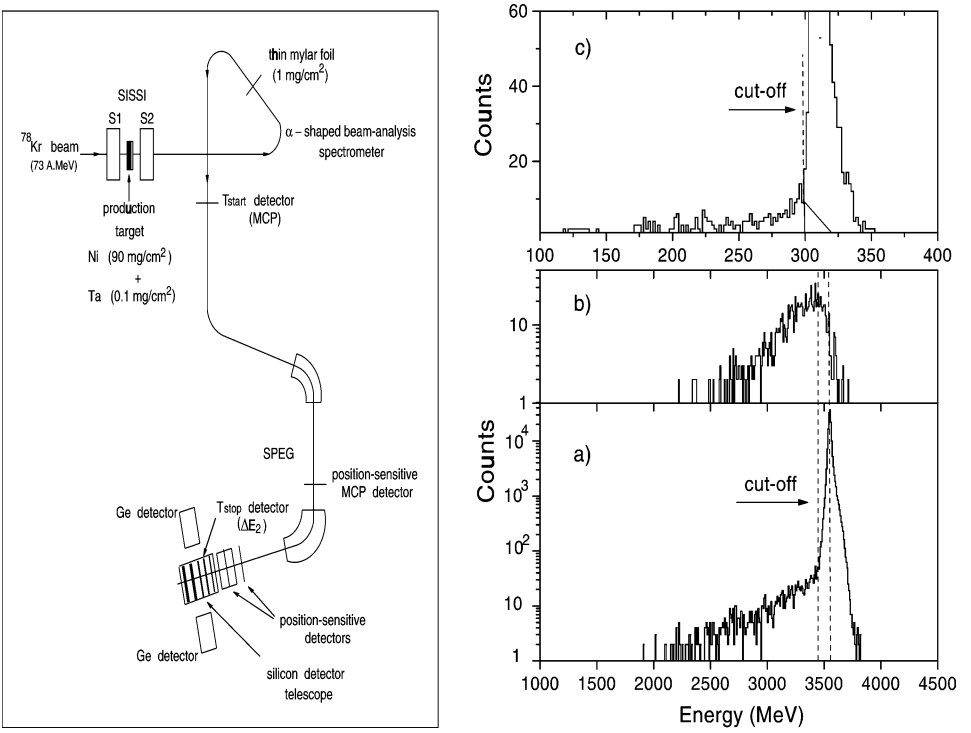

Fig. 1. Left panel: schematic plot of the experimental setup. Right panel: (a) the spectrum of the energy deposited in the whole target/detector system $\Delta E_2 + \Delta E_{xy} + E_{\mathrm{Si(Li)}}$ gated by the identification and by the xy restriction; (b) the coincidence spectrum between the detector telescope (ΔE_2, ΔE_{xy}, $E_{\mathrm{Si(Li)}}$) and the $\bar{E}$, which detects the light particles; (c) the energy spectrum of the ΔE_2 detector gated by the reaction events detected in the Si detector telescope.

resolution energy-loss magnetic spectrometer SPEG [22]. They were detected in the focal plane of SPEG by a cooled silicon telescope formed by three transmission detectors with thickness of 50(ΔE_1), 150(ΔE_2), 163(ΔE_{xy}) μm, followed by a thick Si(Li) detector of 4500 μm, where all ions of interest were stopped. Behind the four Si detectors was located another thick silicon detector ($\bar{E}$, 4000 μm) used to detect the light charged particles (p, d, α, ^{3}He etc.) produced by reactions in the previous detectors.

Particle identification was obtained by combining the energy-loss measurement in the first Si detector (ΔE_1) with the time-of-flight information obtained between a fast micro-channel plate (MCP) detector located at the exit of the α-spectrometer and the Si detector ΔE_2. By restricting events to the central region in the position sensitive element of the telescope ΔE_{xy}, ions scattered from the supports of the preceding detectors were eliminated and the energy resolution was considerably improved.

A purification method based on the stripping of secondary ions (from $q_1 = Z - 1$ to $q_2 = Z$) in a thin mylar foil located between the two sectors of dipoles of the α-spectrometer was used to eliminate light ions without interest. We had a cocktail of secondary beams with about a dozen different nuclides with two different Z values for each $B\rho$ settings. The reaction target was the whole Si telescope behind the thin ΔE_1 detector (used for particle identification). We used two methods in our measurement: one based only on reactions in the thin ΔE_2 detector at a well defined energy E_0, thus allowing the determination of the reaction cross-section at this energy. The other is based on reactions in the whole target/telescope system (ΔE_2, ΔE_{xy}, $E_{\mathrm{Si(Li)}}$) until the complete stopping in the Si(Li) detector. In this case the energy integrated average reaction cross-section is determined.

In Fig. 1(a) we show the spectrum of the energy deposited in the target/detector system ($\Delta E_2 + \Delta E_{xy} + E_{\mathrm{Si(Li)}}$) gated by the identification and by the xy restriction. Events in the low energy tail are due to nuclear reactions with energy loss ($Q \leqslant 0$) in any of the three Si target/detectors, while events in the large peak have not undergone any nuclear reaction. The cut-off, used to separate the peak from the tail, is also shown on the figure, and it is typically at $Q = -150$ MeV. Events corresponding to reactions with Q-values smaller than the energy resolution are contained in the peak and cannot be determined from this spectrum. However, most of the reactions of the proton-rich radioactive projectiles on Silicon are accompanied by light, charged particle emissions, which are detected in the $\bar{E}$ detector. The coincidence spectrum between the sum energy signal of the Si telescope and the $\bar{E}$ detector enables to reveal the reaction events hidden under the elastic peak and take them into account after correcting for the efficiency of the $\bar{E}$ detector. The coincidence spectrum is shown in Fig. 1(b), with reaction events close to $Q = 0$ under the elastic peak and with the low-energy tail somewhat lower than in Fig. 1(a). The efficiency is determined by calculating the ratio of the number of counts in the tail beyond the cutoff (between the $Q = -150$ MeV and $Q = -450$ MeV) in the gated coincidence (Fig. 1(b)) and ungated (Fig. 1(a)) spectra. The efficiency is lower than 1 and depends on the atomic number of the projectile, its values are 0.720(15), 0.678(10), 0.643(13), 0.625(23) and 0.617(43), respectively, for the Ga, Ge, As, Se and Br isotopes. The number of reaction events is given by the sum of the tail ($Q < -150$ MeV) of the ungated spectrum (Fig. 1(a)) with the number of coincidences under the elastic peak ($Q > -150$ MeV) (Fig. 1(b)), divided by the efficiency. The number of reaction events calculated in this way is quite independent of the

position of the cut-off. The efficiency lower than one is due mainly to geometrical effects and due to reaction events with solely neutron and/or γ emission, not detected in $\bar{E}$. The neutron emission with $|Q| \leqslant 100$ MeV was calculated using the CASCADE evaporation code and the contribution for the ^{68}Ge was $\sim$ 2–3%.

We have also measured γ-rays emitted from the reactions using two high efficiency (60%) Ge detectors located perpendicular to the beam direction on opposite sides of the Si-telescope vacuum chamber. The absolute efficiencies ($\sim$ 1.4% at $E_\gamma = 1.33$ MeV) including the geometry, were determined using a calibrated ^{152}Eu source. No prominent γ-rays were detected for most of the nuclides, the only ones were from known isomeric states of beam nuclei as ^{67,69}Ge, ^{69,71}Se, as described in details in a previous work [20]. No low lying excited states of the secondary beam particles were detected. Thus, the inelastic cross-section was low, of the order of the uncertainty and we could assume that interaction and reaction cross-sections are the same, $\sigma_R = \sigma_I$.

In Fig. 1(c) we show the energy spectrum of the ΔE_2 detector gated by the reaction events detected in the target/detector system. The tail corresponds to events which have undergone nuclear reactions in the ΔE_2 detector. The peak corresponds to events without reactions in ΔE_2, which have undergone reactions either in ΔE_{xy} and mainly in the thick Si(Li) detector. The reaction events with Q smaller than the energy resolution and contained in the elastic peak, were taken into account by the inclusion of the triangular area also indicated in Fig. 1(c), in analogy with the coincidence spectrum.

3. Data analysis

3.1. Extraction of reaction cross-sections and reduced strong absorption radii

The reaction probability P_R is defined as the ratio between the number of reaction events and the total number of nuclides incident on the target/detector system. Due to the intrinsic efficiency of Si detectors being unity, the total number of events incident and counted in the Si detectors will be considered the same.

For the ΔE_2 detector, the P_R will be calculated as the ratio between the sum of reaction events (e.g., the tail plus the triangular area in Fig. 1(c)) by the total number of events (e.g., the whole spectrum in Fig. 1(a)). Due to the small thickness of the detector ΔE_2, the reaction probability P_R can be related to σ_R at a well defined energy E_0 by the equation below:

$$\sigma_R(E_0) = -\frac{m \ln(1 - P_R)}{N_A \Delta R}, \tag{1}$$

where m is the atomic mass of Si, N_A is the Avogadro number, ΔR is the thickness of the target/detector ΔE_2, E_0 is the incident energy on the ΔE_2 detector.

For the ions stopping in the whole target/detector system ($\Delta E_2 + \Delta E_{xy} + E_{\mathrm{Si(Li)}}$), the sum of reaction events is given by the number of events in the tail of the ungated spectrum (Fig. 1(a)) summed with the number of coincidences under the elastic peak (Fig. 1(b))

corrected by the above mentioned coincidence efficiency. The relation between P_R and the energy integrated average reaction cross-section is given by

$$\bar{\sigma}_R = \frac{\int_0^{E_0} \sigma_R(E)(dE/dR)^{-1}\,dE}{\int_0^{R_{\max}} dR} = -\frac{m\ln(1-P_R)}{N_A R_{\max}}, \tag{2}$$

where dE/dR is the stopping power and $R_{\max}$ is the range of the ion of interest in Si [23].

The reaction cross sections $\sigma_R(E_0)$ and the energy integrated reaction cross-sections $\bar{\sigma}_R$ measured in this work are presented in Table 1. They were obtained from the reaction probabilities P_R through Eqs. (1) and (2). The uncertainty in the reaction cross-sections comes mainly from the statistical errors and from the uncertainty in the coincidence efficiency with $\bar{E}$ detector. Thus the uncertainty of the energy integrated reaction cross-sections $\bar{\sigma}_R$ is smaller due to the better statistics.

A phenomenological formula was developed by Kox et al. [24], which relates the reaction cross-section σ_R with a reduced strong absorption radius r_0 in the following manner:

$$\sigma_R(E) = \pi r_0^2\left(A_p^{1/3} + A_t^{1/3} + a\frac{A_p^{1/3}A_t^{1/3}}{A_p^{1/3}+A_t^{1/3}} - C(E)\right)^2\left(1-\frac{V_{\mathrm{CB}}}{E_{\mathrm{CM}}}\right), \tag{3}$$

where A_p and A_t are the projectile and target mass numbers, $a = 1.85$ is an asymmetry parameter, $C(E) = 0.31 + 0.014E/A_p$ is an energy dependent transparency term, and V_{CB} is the Coulomb barrier [25]. Using the Kox formula a reduced strong absorption radius r_0 can be deduced, which is independent of the target system and of the projectile energies. For stable nuclei the formula gives a good description of a wide variety of target and projectile systems at different energies with a constant value of $r_0 = 1.1$ fm [24]. The formula was also applied to unstable nuclei and the trend of increasing reduced radii r_0 with neutron excess was found [26].

We have deduced the reduced strong absorption radii r_0 from our reaction cross-sections $\sigma_R(E_0)$ measured in the thin ΔE_2 detector, using the Kox formula (Eq. (3)). As the Kox formula assumes an energy dependence for the reaction cross-section, it can be integrated over the range in the detector/target system (see Eq. (2)), and yields an independent measurement of the reduced strong absorption radius r_0, when compared with the energy integrated reaction cross-section $\bar{\sigma}_R$. The uncertainties in both r_0 values were calculated by error propagation from the uncertainties in σ_R.

The reduced strong absorption radii r_0 obtained, respectively, from $\sigma_R(E_0)$ or from $\bar{\sigma}_R$ using Eqs. (1)–(3), are also presented in Table 1 under columns r_0 (ΔE_2) and r_0 (integrated), respectively. They are also presented on Fig. 2 as a function of $N-Z$ for the five isotopic series studied, Ga ($Z = 31$), Ge ($Z = 32$), As ($Z = 33$), Se ($Z = 34$) and Br ($Z = 35$). The agreement between the r_0 values obtained from both methods is good within the uncertainties. This means that the Kox formula for the energy dependence of σ_R is adequate for these radioactive nuclei. A slightly decreasing trend is verified for all isotopic chains with increasing $N - Z$, important feature which will be discussed below in more detail. We have calculated $\langle r_0\rangle$, the weighted average of both r_0 values, also presented in Table 1. The uncertainties of $\langle r_0\rangle$ were calculated by error propagation from the uncertainties in both r_0 values.

Table 1
Compilation of results of this work on reaction cross-sections and reduced strong absorption radii r_0. The $\langle r_0 \rangle$ is the weighted average of the r_0 (ΔE_2) and r_0 (integrated) values. The reaction cross-section $\langle \sigma_R(E_0) \rangle$ is calculated from $\langle r_0 \rangle$ using the Kox formula. See text for details

Isotope	E_0/A (MeV/nucleon)	$\sigma_R(E_0)$ (mb) (ΔE_2)	$\bar{\sigma}_R$ (mb) integrated	r_0 (fm) (ΔE_2)	r_0 (fm) integrated	$\langle r_0 \rangle$ (fm) average	$\langle \sigma_R(E_0) \rangle$ (mb) average
^{63}Ga	58.6	–	2504(170)	–	1.043(35)	1.043(35)	2620(175)
^{64}Ga	56.8	2441(168)	2406(69)	0.997(38)	1.019(13)	1.017(12)	2514(60)
^{65}Ga	55.1	2591(112)	2373(50)	1.019(25)	1.009(8)	1.010(8)	2505(38)
^{66}Ga	53.4	2547(105)	2324(49)	1.017(24)	0.996(8)	0.998(7)	2471(36)
^{67}Ga	51.8	2231(170)	2309(73)	0.937(40)	0.991(14)	0.985(13)	2430(65)
^{68}Ga	50.3	2476(750)	2304(178)	0.99(15)	0.987(38)	0.987(36)	2460(180)
^{65}Ge	58.6	2510(610)	2450(160)	1.01(12)	1.016(26)	1.016(25)	2511(123)
^{66}Ge	56.9	2814(260)	2554(57)	1.07(5)	1.040(10)	1.041(9)	2668(49)
^{67}Ge	55.2	2476(161)	2437(42)	0.996(32)	1.018(6)	1.017(6)	2569(31)
^{68}Ge	53.6	2511(172)	2401(43)	0.999(34)	1.010(7)	1.010(7)	2558(33)
^{69}Ge	52.0	2294(275)	2312(61)	0.95(6)	0.987(12)	0.985(11)	2456(56)
^{70}Ge	50.5	2389(760)	2453(156)	0.965(15)	1.015(32)	1.013(31)	2620(161)
^{67}As	58.7	–	2535(150)	–	1.025(33)	1.026(32)	2586(154)
^{68}As	56.9	2864(414)	2553(65)	1.07(8)	1.020(13)	1.022(14)	2586(58)
^{69}As	55.3	2379(238)	2444(46)	0.97(5)	1.019(7)	1.018(7)	2600(36)
^{70}As	53.7	2531(272)	2422(49)	1.00(5)	1.007(8)	1.007(8)	2569(41)
^{71}As	52.2	2466(461)	2358(74)	0.98(9)	0.992(14)	0.992(14)	2514(71)
^{72}As	50.7	–	2430(190)	–	1.0136(39)	1.0136(39)	2647(203)
^{69}Se	58.7	2634(741)	2700(284)	1.03(14)	1.067(64)	1.06(6)	2804(306)
^{70}Se	57.0	2795(297)	2700(88)	1.052(56)	1.059(19)	1.058(18)	2811(95)
^{71}Se	55.4	2787(200)	2585(60)	1.046(37)	1.036(11)	1.037(10)	2725(53)
^{72}Se	53.9	2829(490)	2440(64)	1.05(9)	1.006(12)	1.007(12)	2593(62)
^{73}Se	52.4	3156(524)	2445(114)	1.10(9)	1.022(24)	1.028(23)	2725(121)
^{72}Br	57.1	2906(462)	2727(176)	1.068(85)	1.069(34)	1.07(3)	2893(168)
^{73}Br	55.5	2630(272)	2600(111)	1.011(52)	1.040(21)	1.036(18)	2748(95)
^{74}Br	54.0	2863(284)	2557(111)	1.066(52)	1.033(21)	1.038(20)	2781(107)
^{75}Br	52.5	2900(446)	2407(165)	1.063(81)	1.000(33)	1.005(32)	2630(167)

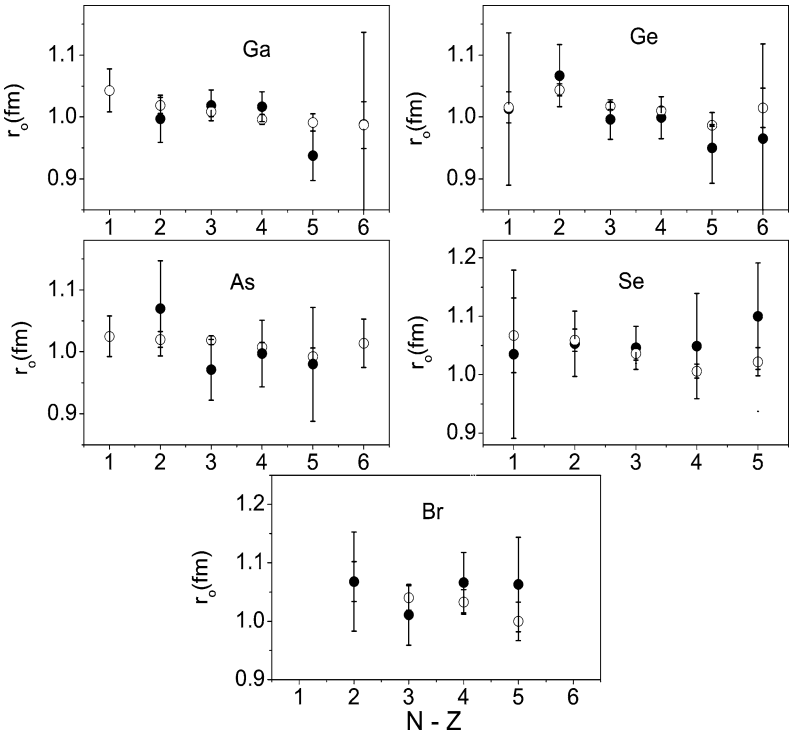

Fig. 2. The reduced strong absorption radii r_0 obtained respectively from $\sigma_R(E_0)$ or from $\bar{\sigma}_R$ are presented as a function of $N - Z$ for the five isotopic series studied. The r_0 (ΔE_2) and r_0 (integrated), respectively, are represented by full dots and circles. The agreement between the r_0 values obtained from both methods is good within the uncertainties.

None of the matter radii of nuclides of the isotopic series studied here were measured previously. Only some of the heaviest, stable nuclides have their charge radii measured by electron scattering and/or muonic atomic X-ray experiments. Unfortunately, the stable nuclides were observed with very low statistics in this experiment. This is due partly to the production cross sections and partly to the charge-state-ratio purification method used. For some heavier nuclides of Ga, Ge and As, the statistics of reaction events in the ΔE_2 detector were too low to allow for the determination of r_0 (ΔE_2) and thus only the r_0 (integrated) could be obtained.

In order to obtain reaction cross-sections for all nuclides studied in this work, with the best possible accuracy, we inverted the problem and used the Kox formula of Eq. (3) at the energy E_0, to obtain reaction cross-sections $\langle\sigma_R(E_0)\rangle$ from the weighted average values of reduced strong absorption radii $\langle r_0\rangle$. The uncertainties of $\langle\sigma_R(E_0)\rangle$ were calculated by error propagation from the uncertainties in $\langle r_0\rangle$. They are presented as last column in Table 1. The agreement between the directly measured $\sigma_R(E_0)$ values and those deduced from $\langle r_0\rangle$ is shown on Fig. 3.

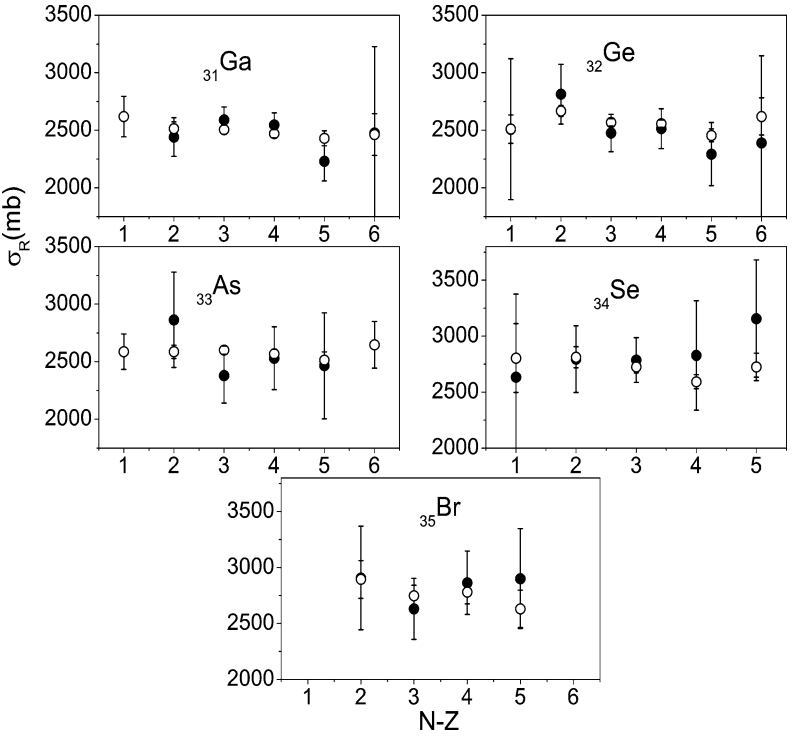

Fig. 3. The reaction cross-sections σ_R (full dots) and $\langle\sigma_R(E_0)\rangle$ (circles) were obtained respectively from direct measurement in ΔE_2 detector and from the weighted average values of reduced strong absorption radii $\langle r_0\rangle$ by inverting the problem and using the Kox formula of Eq. (3) [24].

3.2. Glauber model calculations

The reduced strong absorption radii r_0 obtained in the previous section are not easy to interpret. Our aim is to obtain matter density distributions or at least root-mean-squared (r.m.s.) matter radii ($r_{\rm rms} = \langle r^2\rangle^{1/2}$), which can be compared with theoretical calculations or r.m.s. charge radii. We used the Glauber theory to deduce r.m.s. matter radii from the measured $\langle\sigma_R(E_0)\rangle$ reaction cross-sections. In Glauber theory [27] the reaction cross-section is written as

$$\sigma_R = 2\pi \int_0^\infty b\big[1 - T(b)\big]\,db, \tag{4}$$

where $T(b)$, the squared modulus of the Glauber S-matrix, is the transmission, or transparency of the collision at impact parameter b. One of the simplest approximations to calculate the transparency $T(b)$ is the optical limit, where the N–N cross-section is folded over the static proton and neutron density distributions of the projectile and target nuclei, whose geometric overlap determines the reaction cross-section. The σ_R calculated in this way for stable nuclei using static density distributions determined by electron scattering,

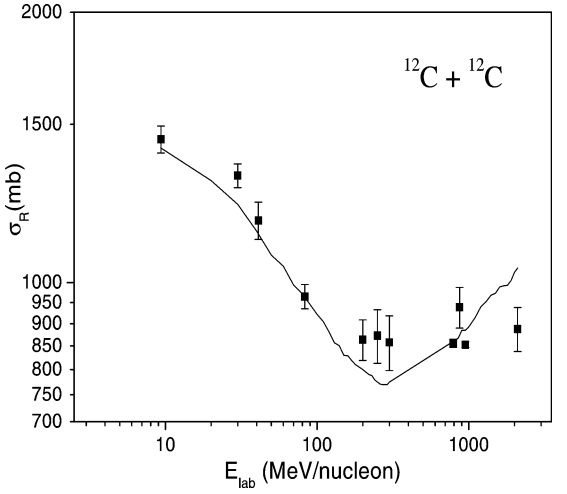

Fig. 4. The experimental reaction cross-sections for the $^{12}C + ^{12}C$ system (full squares) compared to our Glauber model calculations [30] using parameters of the well-known charge density distribution of the ^{12}C nucleus (solid line). A good agreement is verified, mainly in the energy region of our interest ($\sim$ 50–60 MeV/nucleon).

have shown reasonable agreement with data at energies above 20 MeV/nucleon [24,28, 29]. We have used a Glauber model code [30] and parameters of the well-known charge density distribution of the ^{12}C nucleus to calculate the reaction cross-section of the $^{12}C + ^{12}C$ system at energies from 9 to 2100 MeV/nucleon, to compare with existing data. The comparison is shown on Fig. 4. The calculations underestimate by $\sim 10\%$ the cross-section at energies below 30 MeV/nucleon and around 200 MeV/nucleon. The agreement is very good between 40 and 100 MeV/nucleon, which is the energy region of our experimental data.

Recent calculations of Al-Khalili and Tostevin [32] have proved that Glauber theoretical calculations using the static density distribution, or optical limit approximation, underpredict the nuclear matter radii for light, loosely bound halo nuclei. For halo nuclei the granularity of the projectile implies strong spatial correlation between the valence nucleons and core and the collision will appear more transparent. In their adiabatic model they freeze the position co-ordinates for the few-body projectile constituents and obtain larger radii from the same reaction cross-sections.

In our calculations we have assumed that the nuclei are not loosely bound and used the optical limit of the Glauber model, taking the elementary N–N cross-sections from the literature and the two-parameter Fermi type density distributions for protons and neutrons, as

$$\rho_k(r) = \frac{\rho_0}{1 + \exp(r - R_k)/a_k}, \tag{5}$$

where the parameter R_k is the half-density radius, a_k is the surface diffuseness and subscript k indicates protons or neutrons. In order to perform the Glauber model calculations we need the proton and neutron distributions of the projectile and target nuclei.

Proton distributions are not directly measured, but they can be deduced from measured charge distributions. The charge distribution $\rho_{\rm ch}$ is the folding of the point proton distribution ρ_p with the intrinsic charge distribution of the proton in free space $\rho_{{\rm ch}p}$. The parameters of the point proton distribution can be calculated by deconvoluting the charge distribution or by using the formula [7] $\langle r_p^2\rangle = \langle r_{\rm ch}^2\rangle - 0.64$. Recently published [33] systematics for stable nuclei were used for the relation between the charge and proton distribution diffusenesses a_p and $a_{\rm ch}$: $a_p = a_{\rm ch} - 0.03$ fm. Assuming the two-parameter Fermi distribution, we can determine the proton half-density radius R_p from the proton mean squared radius $\langle r_p^2\rangle$ and the diffuseness a_p. For stable $N = Z$ nuclei (the ^{28}Si target nucleus) we can assume that the proton and neutron distributions are equal, thus $R_p = R_n$ and $a_p = a_n$. For the proton-rich radioactive projectiles of this work, we have to make several assumptions to infer the proton and neutron distributions. This assumptions are discussed in detail for each isotopic series in the following.

3.2.1. Proton and neutron distributions of the ^{28}Si target

The charge distribution of the ^{28}Si target nucleus was measured by electron scattering experiments [34] and more recently by muonic atomic transition energies [35]. Using a two-parameter Fermi distribution, the parameters were determined respectively as: root-mean-squared charge radius $\langle r_{\rm ch}^2\rangle^{1/2} = 3.15(4)$ fm and 3.123 fm, half-density charge radius $R_{\rm ch} = 3.14(6)$ and 3.1544(7) fm and charge diffuseness $a_{\rm ch} = 0.537(32)$ and 0.523 fm. These results are also quoted in Table 2. The r.m.s. charge radii of the two measurements agree well and the precision of the latter measurement is much better, for this reason we adopted the more recent values measured by muonic atoms. The parameters of the point proton distribution were calculated by using the formula $\langle r_p^2\rangle = \langle r_{\rm ch}^2\rangle - 0.64$, which yields $\langle r_p^2\rangle^{1/2} = 3.019$ fm for the root-mean-squared proton radius. The above formulae yielded $\langle r_p^2\rangle^{1/2} = 3.019(1)$ fm, $a_p = 0.493$ fm and $R_p = 3.047(6)$ fm for ^{28}Si. We assumed that the proton and neutron distributions were equal for the stable $N = Z = 14$ nucleus ^{28}Si.

3.2.2. Proton and neutron distributions of the proton-rich radioactive projectiles of this work

3.2.2.1. Ge isotopes The only stable nucleus observed in our experiment with measured charge distribution is the ^{70}Ge. The recent results of electron scattering experiments on ^{70}Ge are quoted in the compilation of Fricke et al. [35], and the results are respectively: r.m.s. charge radii $\langle r_{\rm ch}^2\rangle^{1/2} = 4.055(8)$ and 4.043(2) fm, using two-parameter Fermi distribution in the first and Fourier–Bessel analysis in the second one. The values of the half-density radius and diffuseness, when using two-parameter Fermi distribution are respectively: $R_{\rm ch} = 4.430(8)$ fm and $a_{\rm ch} = 0.5807(30)$ fm. The compilation of Fricke [35] also quotes results for nuclear charge radii from muonic atomic transition energies and they yield for the ^{70}Ge the r.m.s. charge radius of $\langle r_{\rm ch}^2\rangle^{1/2} = 4.039$ fm and a half-density radius of $R_{\rm ch} = 4.5687(2)$ fm with a surface diffuseness of $a_{\rm ch} = 0.523$ fm, using the two parameter Fermi distribution. Using all available data up to now for r.m.s. charge radii, Angeli [36] proposes the average value $\langle r_{\rm ch}^2\rangle^{1/2} = 4.0414(12)$ fm. Thus the r.m.s. charge radius is well determined, while an ambiguity persists in the half-density radius and diffuseness of the charge distribution. Using the formulae above explained and adopting

Table 2
Compilation of previously measured charge distributions where index (a) and (b) refers to electron scattering data in Refs. [34,35], (c) to Ref. [38], (d) to muonic X-ray data in Ref. [35] and (e) to compilations of Ref. [36], respectively. The charge distribution diffuseness in (d) is 0.523 fm in all cases. The proton distributions were obtained using formulae quoted in the text

Isotope	R_{ch} (fm)	a_{ch} (fm)	$\sqrt{\langle r^2_{ch}\rangle}$ (fm)	R_{ch} (fm)[(d)]	$\sqrt{\langle r^2_{ch}\rangle}$ (fm)[(d)]	$\sqrt{\langle r^2_{ch}\rangle}$ (fm)[(e)]	R_p (fm)	a_p (fm)	$\sqrt{\langle r^2_p\rangle}$ (fm)
^{28}Si	3.14(6)[(a)]	0.537(32)[(a)]	3.15(4)[(a)]	3.1544	3.123	3.1223(24)	3.047	0.493	3.019
^{70}Ge	4.430(8)[(b)]	0.5807(30)[(b)]	4.055(8)[(b)]	4.5687(2)	4.039	4.0414(12)	4.42	0.55	4.00
^{72}Ge	4.446(8)[(b)]	0.592(3)[(b)]	4.088(8)[(b)]	4.5926(2)	4.055	4.0577(12)	–	–	–
^{73}Ge	–	–	–	4.6015(2)	4.061	4.0634(14)	–	–	–
^{74}Ge	4.454(8)[(b)]	0.608(3)[(b)]	4.126(8)[(b)]	4.6185(2)	4.072	4.0744(12)	–	–	–
^{76}Ge	4.547(8)[(b)]	0.578(3)[(b)]	4.127(8)[(b)]	4.6294(1)	4.080	4.0812(12)	–	–	–
^{69}Ga	–	–	–	4.5066(1)	3.996	3.9973(17)	4.45	0.50	3.92
^{71}Ga	–	–	–	4.5279(1)	4.011	4.0118(18)	4.46	0.50	3.93
^{75}As	–	–	4.102(9)[(c)]	4.6527(1)	4.096	4.0969(19)	4.59	0.50	4.02
^{74}Se	4.387(22)[(b)]	0.6078(7)[(b)]	4.07(2)[(b)]	–	–	4.07(2)	4.50	0.578	3.97
^{76}Se	4.471(11)[(b)]	0.6208(39)[(b)]	4.162(10)[(b)]	4.7162(1)	4.139	4.1397(16)	–	–	–
^{77}Se	–	–	–	4.7163(1)	4.139	4.1397(17)	–	–	–
^{78}Se	4.581(18)[(b)]	0.5729(41)[(b)]	4.138(14)[(b)]	4.7184(1)	4.140	4.1407(17)	–	–	–
^{80}Se	4.667(10)[(b)]	0.5339(42)[(b)]	4.124(10)[(b)]	4.7178(1)	4.140	4.1399(16)	–	–	–
^{82}Se	4.718(11)[(b)]	0.5102(49)[(b)]	4.118(11)[(b)]	4.7179(1)	4.140	4.1399(18)	–	–	–
^{79}Br	–	–	–	4.7519	4.163	4.1630(21)	4.67	0.50	4.085
^{81}Br	–	–	–	4.7474	4.160	4.1599(21)	–	–	–

the $\langle r_{\rm ch}^2\rangle^{1/2} = 4.0414(12)$ fm and $a_{\rm ch} = 0.5807(30)$ fm we calculated the following parameters: $\langle r_p^2\rangle^{1/2} = 4.00$ fm, $a_p = 0.55$ fm and $R_p = 4.42$ fm for the proton distribution of ^{70}Ge. These values are included in Table 2.

Thus, our measured quantities are the reaction cross-sections and the r.m.s. proton radius of the ^{70}Ge. We cannot expect to determine unambiguously the four parameters (R_n, a_n, R_p and a_p) of both, proton and neutron distributions, from our two parameters. In recent works on radioactive Na and Mg isotopes, Suzuki and collaborators [7,37] have proposed a procedure to obtain the r.m.s. matter radii from the reaction cross-sections in a rather unambiguous way. In this procedure some conditions are assumed between the parameters to allow the extraction of the density distributions. Two extreme conditions were applied to see the sensitivity of the final results to the assumptions:

(a) The half-density proton radii for all Ge isotopes were constant $R_p(^{70}\mathrm{Ge}) = R_p(^{A}\mathrm{Ge}) = 4.42$ fm. The half-density neutron radii increase with $N^{1/3}$ and the $T_z = 0$ or 1/2 nuclei had the same neutron and proton half-density radii: $R_p(^{70}\mathrm{Ge}) = R_p(^{65}\mathrm{Ge}) = R_n(^{65}\mathrm{Ge}) = r_{0n}N^{1/3}$ ($T_z = 1/2$ for the ^{65}Ge), thus $r_{0n}(\mathrm{Ge}) = 1.378$ fm. The half-density neutron radii for the Ge isotopes will be given by $R_n(^{A}\mathrm{Ge}) = 1.378N^{1/3} = 1.378(A - 32)^{1/3}$, and the half-density proton radii by $R_p(^{A}\mathrm{Ge}) = 4.42$ fm. After fixing these criteria for the half-density proton and neutron radii, the proton and neutron diffusenesses a_p and a_n were free parameters, in order to reproduce the measured reaction cross-sections through the Glauber model calculations.

(b) We fixed as equal the diffusenesses of the proton and neutron distributions, using the systematics or the measurement of stable isotopes, and varied R_p and R_n independently, in order to reproduce the reaction cross-sections. In the case of Ge isotopes we supposed $a_p(^{A}\mathrm{Ge}) = a_n(^{A}\mathrm{Ge}) = 0.55$ fm (the value obtained for ^{70}Ge).

In assumption (a) the densities change from one nuclide to another because of changes in the diffuseness and the $N^{1/3}$ dependence of R_n, while in assumption (b) the densities change because the half-density radii vary. The reality should be somewhere in-between. We included our Glauber theory calculation into a search routine, where the parameters were varied between given limits and the reaction cross-section was calculated for every ensemble of parameters. We have performed many searches and we could reproduce the reaction cross-sections with several, fairly different proton or neutron distributions. However, the r.m.s. matter radii, which were calculated from these different distributions using a simple averaging formula [7]

$$\langle r_m^2\rangle = \frac{Z}{A}\langle r_p^2\rangle + \frac{N}{A}\langle r_n^2\rangle \tag{6}$$

were very similar. We calculated the average of all r.m.s. matter radii obtained in many searches for each projectile nucleus. The uncertainties in the r.m.s. matter radii were scaled by the uncertainties of the total reaction cross-sections, adopting the same relative errors for both quantities. In Table 3 the r.m.s. matter radii obtained using both assumptions (a) and (b) are presented. The results are fairly close, the difference is always less than the uncertainties. The last column of Table 3 brings the average between both values, which we adopted as our result for r.m.s. matter radii. The uncertainties adopted were again scaled by the uncertainties of the total reaction cross-sections, adopting the same relative errors for both quantities.

3.2.2.2. Ga isotopes The charge radii of the ^{69,71}Ga nuclides were studied through the measurement of the muonic $2p \rightarrow 1s$ transition energies. The results were, respectively, [35] $R_{\rm ch} = 4.5066(1)$, 4.5279(1) fm and $\langle r^2_{\rm ch}\rangle^{1/2} = 3.996$, 4.011 fm with a surface diffuseness of $a_{\rm ch} = 0.523$ fm using the two parameter Fermi distribution. Using the above criteria the parameters of the proton distribution we adopted were respectively $R_p = 4.45$, 4.46 fm and $\langle r^2_p\rangle^{1/2} = 3.92$, 3.93 fm with a surface diffuseness of $a_p = 0.50$ fm.

Using assumption (a) $R_p(^{69}\text{Ga}) = R_p(^{A}\text{Ga}) = 4.45$ fm and $R_p(^{69}\text{Ga}) = R_p(^{63}\text{Ga}) = R_n(^{63}\text{Ga}) = r_{0n}N^{1/3}$ ($T_z = 1/2$ for the ^{63}Ga), thus $r_{0n}(\text{Ga}) = 1.401$ fm. The half-density neutron radii for the Ga isotopes will be given by $R_n(^{A}\text{Ga}) = 1.401N^{1/3} = 1.401(A - 31)^{1/3}$, and the half-density proton radii by $R_p(^{A}\text{Ga}) = 4.45$ fm. After fixing these criteria for the half-density proton and neutron radii, the proton and neutron diffusenesses a_p and a_n were free parameters, in order to reproduce the reaction cross-sections.

In assumption (b) we assumed $a_p = a_n = 0.50$ fm and varied R_p and R_n independently, in order to reproduce the reaction cross-sections. The r.m.s. matter radii were calculated using Eq. (6) and were fairly similar. In Table 3 the r.m.s. matter radii obtained using both assumptions (a) and (b) are presented, together with the average of both.

3.2.2.3. As isotopes The charge radius of the ^{75}As nuclide was studied through the measurement of the muonic $2p \rightarrow 1s$ transition energy. The results were [35] $R_{\rm ch} = 4.6527(1)$ fm and $\langle r^2_{\rm ch}\rangle^{1/2} = 4.096$ fm with a surface diffuseness of $a_{\rm ch} = 0.523$ fm using the two parameter Fermi distribution. Wesolowski [38] quotes $\langle r^2_{\rm ch}\rangle^{1/2} = 4.102(9)$ fm and Angeli [36] 4.0969(19) fm. Using the above criteria and adopting $\langle r^2_{\rm ch}\rangle^{1/2} = 4.0969(19)$ fm and $a_{\rm ch} = 0.523$ fm the parameters of the proton distribution were respectively $\langle r^2_p\rangle^{1/2} = 4.02$ fm with a surface diffuseness of $a_p = 0.50$ fm, yielding half-density proton radius of $R_p = 4.59$ fm.

Using assumption (a) $R_p(^{75}\text{As}) = R_p(^{A}\text{As}) = 4.59$ fm and $R_p(^{75}\text{As}) = R_p(^{67}\text{As}) = R_n(^{67}\text{As}) = r_{0n}N^{1/3}$ ($T_z = 1/2$ for the ^{67}As), thus $r_{0n}(\text{As}) = 1.417$ fm. The half-density neutron radii for the As isotopes will be given by $R_n(^{A}\text{As}) = 1.417N^{1/3} = 1.417(A - 33)^{1/3}$, and the half-density proton radii by $R_p(^{A}\text{As}) = 4.59$ fm. After fixing these criteria for the half-density proton and neutron radii, the proton and neutron diffusenesses a_p and a_n were free parameters, in order to reproduce the reaction cross-sections.

In assumption (b) we assumed $a_p = a_n = 0.50$ fm and varied R_p and R_n independently, in order to reproduce the reaction cross-sections. The r.m.s. matter radii were calculated using Eq. (6) and were fairly similar. In Table 3 the r.m.s. matter radii obtained using both assumptions (a) and (b) are presented, together with the average of both.

3.2.2.4. Se isotopes The charge radii of the ^{74,76,77,78,80,82}Se nuclides were studied through the measurement of electron scattering and muonic $2p \rightarrow 1s$ transition energies. The results of both methods are quoted in the compilation of Fricke et al. [35] and presented on Table 2.

The results of electron scattering experiments yield for ^{74,76,78,80,82}Se the r.m.s. charge radii $\langle r^2_{\rm ch}\rangle^{1/2} = 4.07(2)$, 4.162(10), 4.138(14), 4.124(10) and 4.118(11) fm, using the two parameter Fermi distribution. For the ^{74}Se the diffuseness is 0.6078(7) and the half-density charge radius 4.387(22) fm. The r.m.s. charge radii from muonic atomic transition

energies for ^{76,77,78,80,82}Se nuclides are $\langle r^2_{\rm ch}\rangle^{1/2} = 4.139, 4.139, 4.140, 4.140$ and 4.140 fm respectively with a surface diffuseness of $a_{\rm ch} = 0.523$ fm, using the two parameter Fermi distribution. Using all available data up to now for r.m.s. charge radii, Angeli [36] proposes $\langle r^2_{\rm ch}\rangle^{1/2} = 4.07(2)$, 4.1397(16), 4.1397(16), 4.1407(17), 4.1399(16) and 4.1399(18) fm, respectively. Thus the r.m.s. charge radii are fairly well determined. We adopted the measured parameters for the charge distribution of ^{74}Se and obtained the following parameters: $\langle r^2_p\rangle^{1/2} = 3.97$ fm, $a_p = 0.578$ fm and $R_p = 4.50$ fm for the proton distribution of ^{74}Se, using the same criteria above explained. These values are included in Table 2.

Using assumption (a) $R_p(^{74}\text{Se}) = R_p(^{A}\text{Se}) = 4.50$ fm and $R_p(^{74}\text{Se}) = R_p(^{69}\text{Se}) = R_n(^{69}\text{Se}) = r_{0n}N^{1/3}$ ($T_z = 1/2$ for the ^{69}Se), thus $r_{0n}(\text{Se}) = 1.370$ fm. The half-density neutron radii for the Se isotopes will be given by $R_n(^{A}\text{Se}) = 1.370N^{1/3} = 1.370(A - 34)^{1/3}$, and the half-density proton radii by $R_p(^{A}\text{Se}) = 4.50$ fm.

After fixing these criteria for the half-density proton and neutron radii, the proton and neutron diffusenesses a_p and a_n were free parameters, in order to reproduce the reaction cross-sections.

In assumption (b) we assumed $a_p = a_n = 0.578$ fm and varied R_p and R_n independently, in order to reproduce the reaction cross-sections. The r.m.s. matter radii were calculated using Eq. (6) and were fairly similar. In Table 3 the r.m.s. matter radii obtained using both assumptions (a) and (b) are presented, together with the average of both.

3.2.2.5. Br isotopes The charge radii of the ^{79,81}Br nuclides were studied through the measurement of the muonic $2p \to 1s$ transition energy. The results were respectively $R_{\rm ch} = 4.7519(1)$, 4.7474(1) fm and $\langle r^2_{\rm ch}\rangle^{1/2} = 4.163$ and 4.160 fm with a surface diffuseness of $a_{\rm ch} = 0.523$ fm using the two parameter Fermi distribution [35]. Using the above criteria the parameters of the proton distribution of ^{79}Br were respectively $R_p = 4.67$ fm and $\langle r^2_p\rangle^{1/2} = 4.085$ fm with a surface diffuseness of $a_p = 0.50$ fm.

Using assumption (a) $R_p(^{79}\text{Br}) = R_p(^{A}\text{Br}) = 4.67$ fm and $R_p(^{79}\text{Br}) = R_p(^{72}\text{Br}) = R_n(^{72}\text{Br}) = r_{0n}N^{1/3}$ ($T_z = 1$ for the ^{72}Br), thus $r_{0n}(\text{Br}) = 1.370$ fm. The half-density neutron radii for the Br isotopes will be given by $R_n(^{A}\text{Br}) = 1.370N^{1/3} = 1.370(A - 35)^{1/3}$, and the half-density proton radii by $R_p(^{A}\text{Br}) = 4.67$ fm. After fixing these criteria for the half-density proton and neutron radii, the proton and neutron diffusenesses a_p and a_n were free parameters, in order to reproduce the reaction cross-sections and the measured charge radii.

In assumption (b) we assumed $a_p = a_n = 0.50$ fm and varied R_p and R_n independently, in order to reproduce the reaction cross-sections. The r.m.s. matter radii were calculated using Eq. (6) and were fairly similar. In Table 3 the r.m.s. matter radii obtained using both assumptions (a) and (b) are presented, together with the average of both.

4. Discussion of results

4.1. Variation of the radius with the neutron excess $N - Z$

Using assumptions (a) and (b) described in the preceding section and varying the free parameters in the Glauber model calculations the reaction cross-sections were fitted. From

Table 3
Compilation of results of Glauber calculations using assumptions (a) and (b) to obtain r.m.s. matter radii. The last column contains the average of preceding columns and represents the final r.m.s. matter radii of this work. See text for details on parameters used

Isotope	E_0/A (MeV)	$\langle\sigma_R(E_0)\rangle$ (mb) average	$\langle r_m^2\rangle^{1/2}$ (a)	$\langle r_m^2\rangle^{1/2}$ (b)	$\langle r_m^2\rangle^{1/2}$ average
^{63}Ga	58.6	2620(175)	3.90(26)	3.915(26)	3.91(26)
^{64}Ga	56.8	2514(60)	3.78(10)	3.71(10)	3.75(10)
^{65}Ga	55.1	2505(38)	3.78(8)	3.67(8)	3.73(8)
^{66}Ga	53.4	2471(36)	3.74(8)	3.60(8)	3.68(8)
^{67}Ga	51.8	2430(65)	3.68(10)	3.56(10)	3.62(10)
^{68}Ga	50.3	2460(182)	3.72(27)	3.58(27)	3.65(27)
^{65}Ge	58.6	2511(120)	3.66(17)	3.54(17)	3.60(17)
^{66}Ge	56.9	2668(49)	3.837(7)	3.74(7)	3.80(7)
^{67}Ge	55.2	2569(31)	3.72(5)	3.62(5)	3.67(5)
^{68}Ge	53.6	2558(33)	3.686(5)	3.54(5)	3.61(5)
^{69}Ge	52.0	2456(56)	3.57(10)	3.43(10)	3.50(10)
^{70}Ge	50.5	2619(161)	3.75(20)	3.61(22)	3.68(22)
^{67}As	58.7	2586(153)	3.85(22)	3.82(22)	3.84(22)
^{68}As	56.9	2586(58)	3.81(8)	3.80(8)	3.81(8)
^{69}As	55.3	2600(36)	3.84(5)	3.82(5)	3.83(5)
^{70}As	53.7	2570(41)	3.81(6)	3.74(6)	3.78(6)
^{71}As	52.2	2514(71)	3.76(11)	3.67(11)	3.72(11)
^{72}As	50.7	2647(203)	3.84(30)	3.86(30)	3.85(30)
^{69}Se	58.7	2804(306)	4.06(40)	4.11(40)	4.08(40)
^{70}Se	57.0	2811(95)	4.04(12)	4.06(12)	4.05(12)
^{71}Se	55.4	2725(53)	3.97(8)	3.97(8)	3.97(8)
^{72}Se	53.9	2593(62)	3.82(9)	3.79(9)	3.81(9)
^{73}Se	52.4	2725(121)	3.93(17)	3.90(17)	3.92(17)
^{72}Br	57.1	3893(168)	4.15(24)	4.30(24)	4.22(24)
^{73}Br	55.5	2747(95)	4.01(14)	4.06(14)	4.04(14)
^{74}Br	54.0	2781(107)	4.033(15)	4.08(15)	4.06(15)
^{75}Br	52.5	2630(167)	3.90(25)	3.80(25)	3.85(25)

the best-fit parameters we calculated the r.m.s. matter radii presented in Table 3. The r.m.s. matter radii obtained by the two assumptions were similar, in most cases the difference between them was much smaller than their uncertainty. The last column of Table 3 brings the average of both values, which we adopted as our result for r.m.s. matter radius. These radii are presented as a function of $N - Z$ on Fig. 5, using full dots to represent them. A decreasing tendency of the radii with increasing neutron number $N - Z$ can be observed for most of isotopic chains. We also show on this figure, presented by dotted lines, the values of the nuclear radius given by $R = 0.95A^{1/3}$, supposing a constant reduced radius $r_0 = 0.95$ fm and the usual mass dependence $A^{1/3}$. The purpose is to compare the expected behaviour with increasing N (and A) with the observed behaviour, which is inverse.

We also include in Fig. 5 the r.m.s. charge radii of the Kr isotopic chain, using hollow circles to represent them. They were measured at ISOLDE by laser spectroscopy [39]. They present an increasing feature for increasing $N - Z$ between 0 and 4 and a decreasing

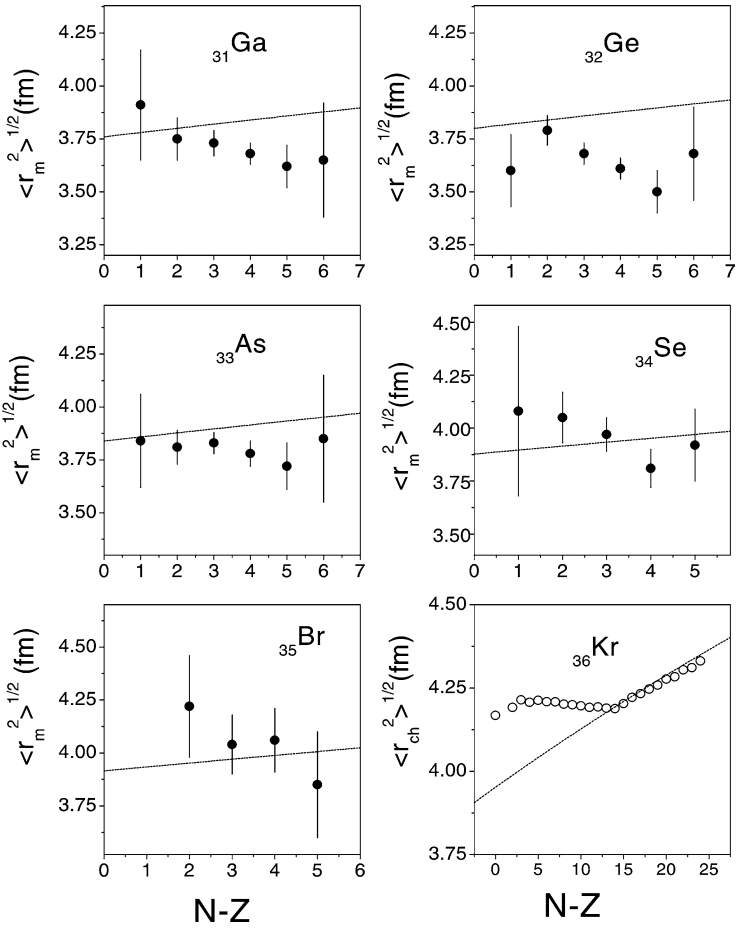

Fig. 5. The r.m.s. matter radii (full dots) obtained from Glauber model calculations for Ga, Ge, As, Se and Br isotopes from reaction cross-sections determined in this work (see text). The r.m.s. charge radii of Kr are also indicated for comparison by circles [39]. The dashed lines indicate the nuclear radius supposing $R = 0.95A^{1/3}$, which means a constant reduced radius $r_0 = 0.95$ fm.

behaviour for $N - Z$ increasing from 4 to 14. The radial variation of the Kr r.m.s. charge radii with neutron number is much slower then the variation we observe (observe the scale of the figures). For $N - Z \geqslant 14$ ($N \geqslant 50$) the Kr radii again increase. The variations of the Kr r.m.s. charge radii were completely explained by deformation effects in the middle shell nuclides, and also reproduced by relativistic mean field calculations [40]. However the increase in radius for $N - Z \geqslant 14$ ($N \geqslant 50$) can be fully accounted by the mass effect.

We try also to clarify if the variation in our matter radii is due to deformation effects, to shell effects (angular momentum of the valence nucleons) or separation energy effects.

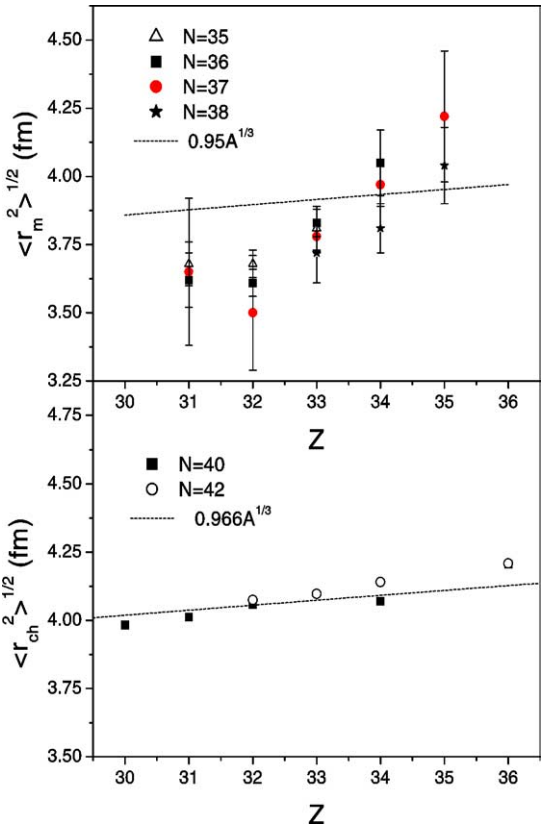

Fig. 6. Upper panel: the r.m.s. matter radii for constant N, as a function of the atomic number Z, obtained for radioactive proton-rich nuclei in this measurement. The dashed line indicates the nuclear radius supposing $R = 0.95A^{1/3}$, which means a constant reduced radius $r_0 = 0.95$ fm. Lower panel: the r.m.s. charge radii for constant N, as a function of the atomic number Z, measured by electron scattering on stable nuclei, obtained from tables of Refs. [34–36] (see text). The dashed line indicates the nuclear radius supposing $R = 0.966A^{1/3}$.

4.2. Variation of the radius with the atomic number Z

The correlation of the nuclear radius with atomic number Z was also considered. In Fig. 6 we present the r.m.s. matter radii as a function of Z for the radioactive proton-rich nuclei we studied at fixed neutron numbers, $N = 35$, 36, 37 and 38. We also indicate with a dotted line the mass effect, plotting $R = 0.95A^{1/3}$. The matter radii increase more strongly with Z then the $A^{1/3}$ effect, the same tendency is observed for all N values. If we plot the r.m.s. charge radii of the stable Zn, Ga, Ge, As, Se and Kr isotopes as a function of Z, for fixed neutron numbers $N = 40$, 42 the result is a much slower increase with Z, fairly well reproduced by $0.966A^{1/3}$. This result is shown in lower panel of Fig. 6. Thus for the unstable, proton rich nuclides an anomalous increase of the r.m.s. matter radius with Z is verified.

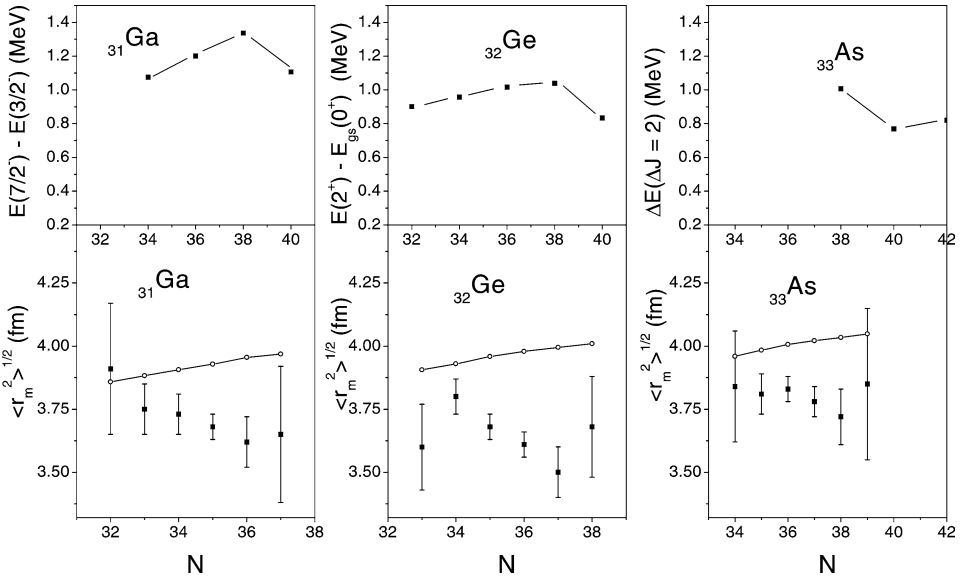

Fig. 7. Lower panels: the r.m.s. matter radii (full squares) of the Ga, Ge and As isotopes as a function of neutron number N. We also show on these figures, presented by hollow circles and solid lines, the values of the nuclear matter radius obtained from relativistic Hartree–Bogoliubov calculations [42]. Upper panels: the excitation energies of first 2^+ or $J = J_{gs} + 2$ state as a function of N [41].

4.3. Variation of the radius with the deformation

In order to clarify if the variation in our matter radii is due to deformation effects, we compare the N dependence of the radius with the N dependence of the deformation. Instead of using deformation parameters or quadrupole moments, not known for all isotopes of interest, we will compare with the excitation energy of the first 2^+ state for even–even nuclei, or with the excitation energy of the first excited state with $J = J_{gs} + 2$ for odd–even nuclei [41]. It is well known that, the higher this excitation energy, the less collective or the less deformed is the nucleus. In Figs. 7 and 8 we present three panels each, respectively the Ga, Ge and As isotopic series on Fig. 7 and the Se, Br and Kr on Fig. 8: on the lower part of the panels the $\langle r_m^2 \rangle^{1/2}$ r.m.s. matter radii are shown, as a function of the neutron number N.

We also show on these figures, presented by hollow circles and solid lines, the values of the nuclear matter radius obtained from relativistic Hartree–Bogoliubov calculations. The calculations were performed using the TMA parameterization of the mean field and a zero-range relativistic pairing interaction with no cutoff [42]. The strength of the pairing interaction was adjusted to reproduce the average trend of the pairing in the region. Blocking was included in the cases of odd neutron and/or proton number. The experimental binding energies were reproduced to about 1 MeV by the calculations. Axially symmetric deformation was permitted in the calculations, which furnished a quadrupole deformation, either oblate or prolate, of about 0.2, in all cases. The calculations predict that these neutron-deficient nuclei are deformed, while the excitation energy of the first 2^+ state is

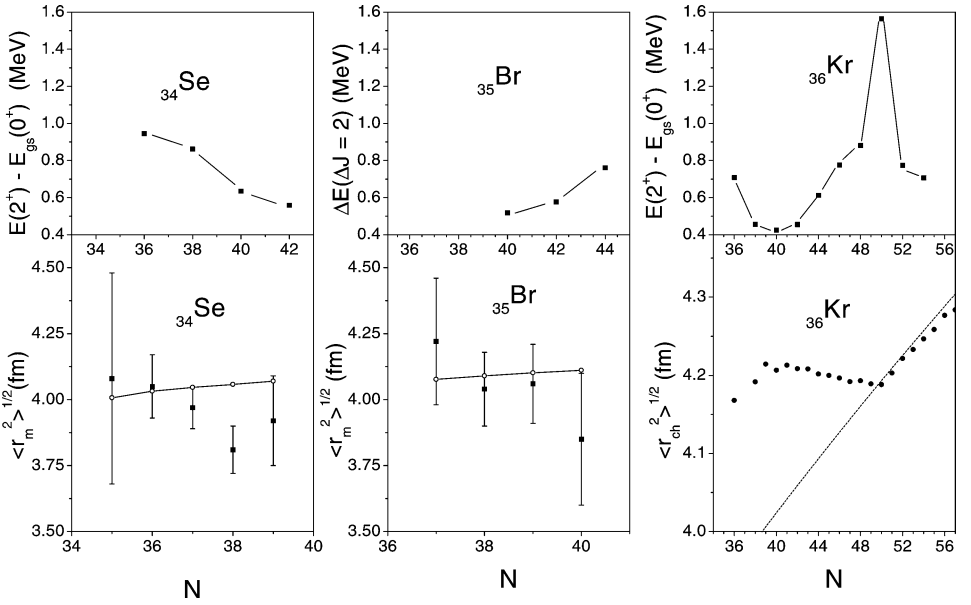

Fig. 8. Lower panels: the r.m.s. matter radii (full squares) of the Se, Br isotopes as a function of neutron number N. For the Kr isotopes the r.m.s. charge radii were plotted (dots) for comparison [39]. Note the difference in scale. We also show on these figures, presented by hollow circles and solid lines, the values of the nuclear matter radius obtained from relativistic Hartree–Bogoliubov calculations [42]. Upper panels: the excitation energies of first 2^+ or $J = J_{gs} + 2$ state as a function of N [41].

more compatible with spherical shapes. The calculated matter radii do not present neither the dependence with N nor the strong Z-dependence.

For the Kr isotopes we plot the r.m.s. charge radii presented by dots. On the top, the excitation energies of the first 2^+ state for the even–even $_{32}$Ge, $_{34}$Se and $_{36}$Kr nuclides, or the excitation energy of the first $J = J_{gs} + 2$ state of the odd–even $_{31}$Ga, $_{33}$As and $_{35}$Br nuclides are presented as a function of N. On Fig. 7 the excitation energies of Ga and Ge have a similar pattern, a peak at $N = 38$, corresponding to spherical character for ^{69}Ga and ^{70}Ge. The magic number $N = 40$ corresponds to fairly high excitation energy for $Z = 31$, 32. For decreasing neutron numbers, $N = 36$, 34, 32, the excitation energies of Ga and Ge decrease very little, indicating that close to the $N = Z$ line these nuclides are still fairly spherical. These facts indicate that the Ga and Ge nuclides, which present an increase in the radial extension with decreasing neutron number very probably still have spherical shapes and the increase is not due to deformation.

For the As chain no excitation energies are available for $N < 38$. For decreasing $N = 42$, 40, 38 the excitation energies increase, suggesting again spherical form in the region close to the $N = Z$ line.

In Fig. 8 the excitation energies of the Se isotopes have a similar behaviour but shifted in N, the peak (spherical shape) is around $N = 36$ and the minimum (deformed shape) at $N = 42$. Thus with decreasing N between 42 and 36, the Se isotopes become more spherical and any increase in the radial extension should not be credited to deformation

effects. For the Br isotopes, no excitation energies are available for $N < 40$. For the Kr isotopes, the Fig. 8 is very revealing. First of all, for $N \geqslant 50$ the charge radii increase in the same rate as $A^{1/3}$, suggesting that the increase in the r.m.s. radii in this region can be explained by the mass increase. The r.m.s. charge radii present a minimum at the magic number $N = 50$, where the excitation energy presents a strong peak. The increase in radius with decreasing N between $N = 50$ and 40 is correlated with the deformation effect, the excitation energies decrease while the radii increase, the maximum of deformation occurring for $N = 40$. For $N < 40$ the excitation energies increase and the radii decrease again, but again it can be explained by the mass effect.

Thus we can conclude that for the Ga, Ge, As, Se and Br isotopes the observed increase in radial extension with decreasing N is not correlated with an increase in deformation, the increase in their radii occurs while the nuclei remain spherical.

4.4. Variation of the radius with the separation energy

The correlation of the nuclear radius with binding energy or separation energy is also an important issue. A strong correlation was observed between the difference in proton and neutron separation energy $S_p - S_n$ and the difference between r.m.s. proton and neutron radii $\langle r_p^2 \rangle^{1/2} - \langle r_n^2 \rangle^{1/2}$ for some neutron-rich and proton rich isotopic chains. This correlation indicates an increasing neutron skin for the neutron-rich Na isotopes and also for some light neutron-rich nuclei and a proton skin for the ^{31}Ar, with the skin thickness decreasing with increasing separation energies for the Ar isotopes [17,31,37,43]. This correlation suggests that the driving force for the formation of skin phenomenon is mainly the difference between the proton and neutron Fermi-energies.

In our case we have the r.m.s. matter radii, but not the proton and neutron radii separately, thus we cannot calculate any parameter related to the skin. We plot on Fig. 9 the matter radii as a function of the proton separation energy. This plot shows no clear correlation between the separation energy and the radii, probably because it is the total matter radius which is plotted.

4.5. Variation of the radius with shell effects

The Ga isotopes ($Z = 31$) have three protons outside the $Z = 28$ closed shell. The ground state spins of the odd–even Ga isotopes are $J^\pi = 3/2^-$, indicating that the last valence proton for the $^{63-71}$Ga isotopes is in the $2p_{3/2}$ shell. The number of neutrons varies from $N = 32$ to 37, thus they are mainly filling the $1f_{5/2}$ shell. The centrifugal barrier is thus larger for the neutrons than for the protons. By increasing the number of neutrons the protons become more tightly bound and have their radius decreased, while the neutron radius does not seem to increase much may be due to the stronger centrifugal barrier, to which the $1f_{5/2}$ neutrons are submitted. This could explain the reduction of the total matter radius with the increase of neutron number N.

For the odd–even Ge isotopes we can get information on the neutron filling: the ground-state of the ^{65}Ge ($N = 33$) is $J^\pi = 3/2^-$, and of the ^{67}Ge ($N = 35$) $J^\pi = 1/2^-$, indicating that their valence neutrons still are in the $2p$ shell instead of the $1f$ shell, thus having smaller centrifugal barrier. For the ^{69}Ge ($N = 37$) the ground state spin is $5/2^-$, indicating

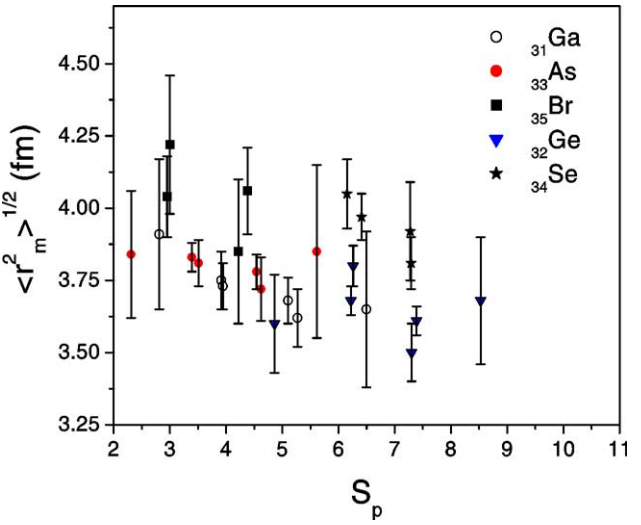

Fig. 9. The r.m.s. matter radii of the Ga, Ge, As, Se and Br isotopes measured in this work are presented as a function of the proton separation energy [41].

the $1f$ shell. Again the protons are in the $2p$ shell and adding neutrons just makes the proton radius get reduced, while the neutron radius can even decrease, when we go from p-shell valence neutrons to f-shell.

For the odd–even As isotopes all ground state spins are $5/2^-$ suggesting that the valence proton is in the $1f_{5/2}$ shell. The decrease of the r.m.s. matter radius with increasing neutron number is less pronounced for the As isotopes than the Ga and Ge isotopes, may be due to appurtenance to the $l = 3$ shell for the protons.

For the odd–even Se isotopes we can get information on the neutron filling: the ground-state of the ^{69}Se ($N = 35$) is $J^\pi = 1/2^-, 3/2^-$, indicating that the valence neutron is still in the $2p$ shell, thus having smaller centrifugal barrier. For the ^{71}Se ($N = 37$) and ^{73}Se ($N = 39$) the ground state spins are $5/2^-$ and $9/2^+$, indicating appurtenance to the $1f$ and $1g$ shell.

The correlation of the total matter radius with shell-effects suggests that the centrifugal barrier of the valence protons and neutrons can be responsible for the radial extension.

4.6. Q-value dependence of the reaction cross-section

In our method, contrarily to the transmission method, the energy spectrum of the projectile is measured, allowing to determine the Q-value dependence of the reaction cross-section. We present on Fig. 10, the sum energy spectra (dotted line) for 4 nuclides, the ^{64,67}Ga and ^{70,73}Se, representing, respectively, a low and a higher Z system, with a proton-rich and a close to stability nucleus. The coincidence spectra are superimposed and the cutoff at $Q = -150$ MeV is also indicated by a vertical line. In the lower panel we show the coincidence spectra on a more expanded scale. The area under the elastic peak in the coincidence spectra ($Q > -150$ MeV) depend strongly on $N - Z$ and also on Z, they

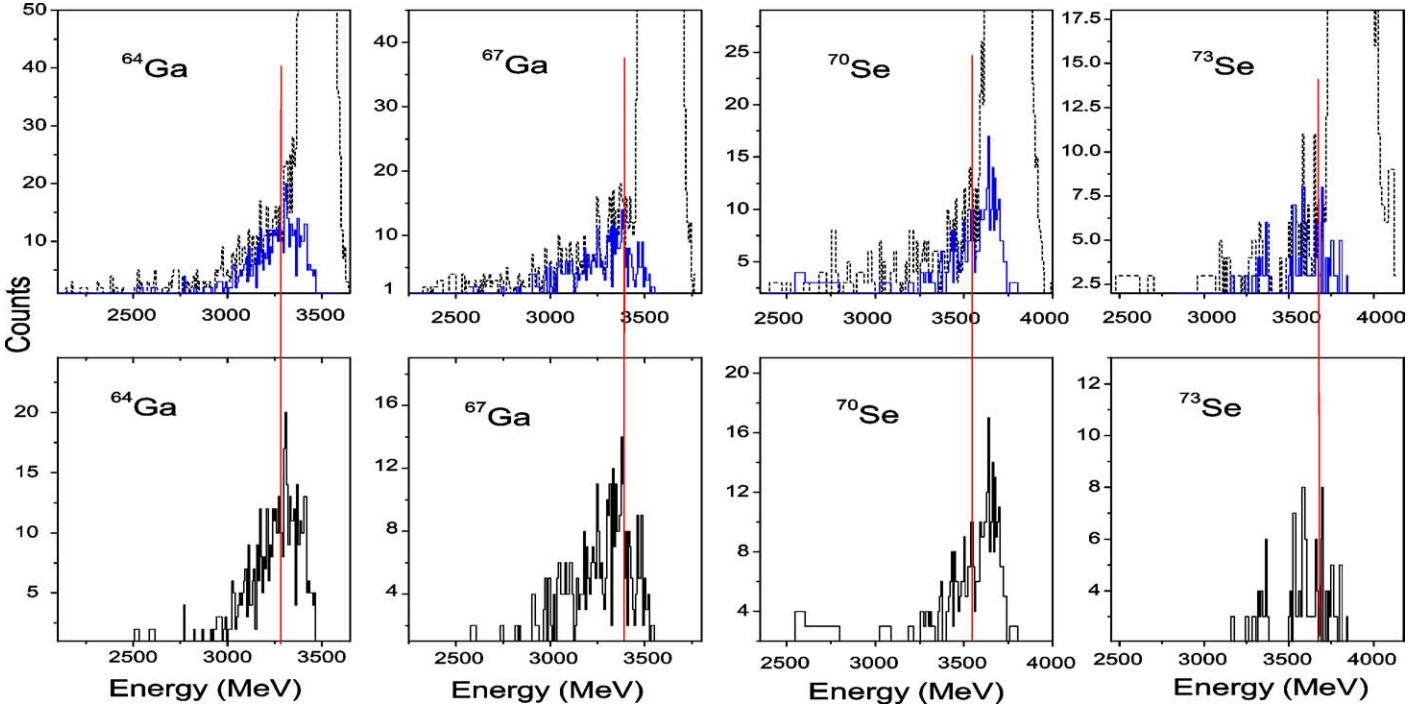

Fig. 10. Upper panel: the ungated sum energy spectra (dotted line) of ^{64,67}Ga and ^{70,73}Se projectiles, together with the gated coincidence spectra (solid line). The cut-off at $Q = -150$ MeV is also indicated by a solid vertical line. Lower panel: the coincidence spectra are shown with an expanded scale. See text.

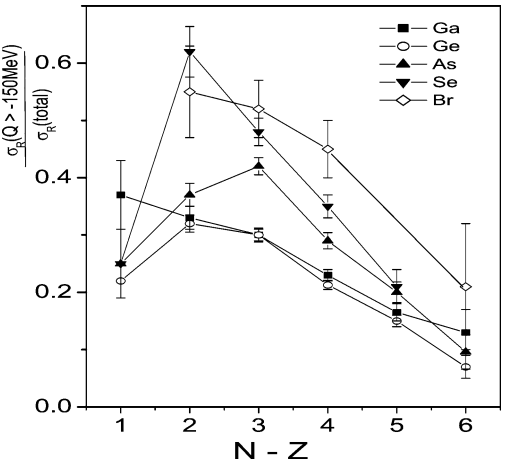

Fig. 11. The ratio of the reaction cross-section leading to final states with $Q > -150$ MeV over the total reaction cross-section is presented as a function of $N - Z$ for the different isotopic series of this work.

are quite small for the close to stability line nuclei (^{67}Ga and ^{73}Se), and they are large for the more exotic nuclei (^{64}Ga and ^{70}Se). We calculated the reaction cross-section summed over final states with $Q > -150$ MeV and also the total reaction cross-section, summed over all final states. The ratio of these two quantities measures the contribution of lower lying final states to the total cross-section.

We plot on Fig. 11 this ratio for all nuclides studied in our work, as a function of $N - Z$, using different symbols for each isotopic series. We can verify a strong correlation with $N - Z$ and also with Z. This ratio presents a maximum around $N - Z = 2$, decreasing strongly (from 0.6 to 0.2) when we approach the stability line. The ratio increases with Z, being around 0.3 as maximum value for Ga and Ge and increasing to 0.6 for Se and Br. May be the higher contribution of low Q-value states indicates some enhanced collectiveness for the most exotic species when compared to more stable species.

5. Conclusion

In summary, we have measured the reaction cross-sections σ_R of proton-rich nuclides of the Ga, Ge, As, Se and Br isotopic chains at intermediate energies. The target/detector system was the Si telescope, where the radioactive ions were stopped. We obtained the reaction cross-section from reactions in a thin ΔE detector and the energy integrated cross-section in the whole telescope. The inelastic cross-section, measured in Ge detectors, was fairly low, allowing to neglect it and assume $\sigma_R = \sigma_I$. We used Glauber model calculations to obtain rms matter radii from the measured reaction cross-sections. A clear correlation of the total r.m.s. matter radii with neutron number N and with proton number Z was verified. The radii decrease with increasing N, and increase strongly with increasing Z. None of the isotopic series studied present an increase in radius with increasing N. The

change in radius is not due to deformations. No clear correlation of the total r.m.s. matter radius with proton separation energy was verified in our data.

For all nuclides studied in this work $N \geqslant Z$ and due to fairly large Z values the Coulomb barrier is also high. The existence of proton skin is very unlikely in this context. However the observed features of decreasing matter radii with increasing N, and strong increase in the radii with increasing Z are difficult to explain supposing a larger neutron radius than proton radius.

One possible explanation for the radial variation is the difference in centrifugal barriers due to the different orbital angular momenta for protons and neutrons, filling respectively mainly the $2p$ shell or the $1f$ shell.

Acknowledgements

G.F.L, A.L.-S. and R.L. wish to thank the Fundação de Amparo à Pesquisa do Estado de São Paulo (FAPESP) and the Conselho Nacional de Desenvolvimento Científico e Tecnológico (CNPq) for financial support. We thank Dr. L.C. Chamon and Isao Tanihata for fruitful discussions. The assistance of the SPEG crew (J.F. Libin and P. Gagnant) in setting up the experiment is also fully acknowledged.

References

[1] P.G. Hansen, A.S. Jensen, B. Jonson, Annu. Rev. Nucl. Part. Sci. 45 (1995) 505.
[2] I. Tanihata, et al., Phys. Lett. B 160 (1985) 380.
[3] T. Kobayashi, et al., Phys. Rev. Lett. 60 (1988) 2599.
[4] R. Neugart, Eur. Phys. J. A 15 (2002) 35.
[5] I. Tanihata, et al., Phys. Lett. B 289 (1992) 261.
[6] G.D. Alkhazov, et al., Phys. Rev. Lett. 78 (1997) 2313.
[7] T. Suzuki, et al., Phys. Rev. Lett. 75 (1995) 3241.
[8] A. Ozawa, T. Suzuki, I. Tanihata, Nucl. Phys. A 693 (2001) 32.
[9] W. Schwab, et al., Z. Phys. A 350 (1995) 283.
[10] J.H. Kelley, et al., Phys. Rev. Lett. 77 (1996) 5020.
[11] F. Negoita, et al., Phys. Rev. C 54 (1996) 1787.
[12] M.H. Smedberg, et al., Phys. Lett. B 452 (1999) 1.
[13] A.M. Mukhamedzanov, N.K. Timofeyuk, JETP Lett. 51 (1990) 282.
[14] H. Esbensen, G.F. Bertsch, Phys. Rev. C 59 (1999) 3240.
[15] A. Navin, et al., Phys. Rev. Lett. 81 (1997) 5089.
[16] R. Kanungo, et al., Nucl. Phys. A 734 (2004) 337.
[17] A. Ozawa, et al., Nucl. Phys. A 709 (2002) 60.
[18] W. Mittig, Nucl. Phys. News 1 (1990) 30.
[19] M. Chartier, et al., Nucl. Phys. A 637 (1998) 3.
[20] G.F. Lima, et al., Phys. Rev. C 65 (2002) 044618.
[21] W. Mittig, et al., Nucl. Phys. A 616 (1997) 329c.
[22] L. Bianchi, et al., Nucl. Instrum. Methods Phys. Res. A 276 (1989) 509.
[23] F. Hubert, R. Bimbot, H. Gauvin, At. Data Nucl. Data Tables 46 (1990) 1.
[24] S. Kox, et al., Phys. Rev. C 35 (1987) 1678.
[25] A.C.C. Villari, et al., Phys. Lett. B 268 (1991) 345.
[26] W. Mittig, et al., Phys. Rev. Lett. 59 (1987) 1889.

[27] R.J. Glauber, in: W.E. Brittin (Ed.), Lectures in Theoretical Physics, vol. 1, Interscience, New York, 1959, p. 315.
[28] S.K. Charagi, S.K. Gupta, Phys. Rev. C 41 (1990) 1610.
[29] P.J. Karol, Phys. Rev. C 11 (1975) 1203.
[30] B. Fernandez, Glauber model code, private communication.
[31] A. Ozawa, et al., Nucl. Phys. A 608 (1996) 63.
[32] J.S. Al-Khalili, J.A. Tostevin, Phys. Rev. Lett. 76 (1996) 3903.
[33] L.C. Chamon, et al., Phys. Rev. C 66 (2002) 014610.
[34] H. De Vries, C.W. Jager, C. De Vries, At. Data Nucl. Data Tables 36 (1987) 495.
[35] G. Fricke, et al., At. Data Nucl. Data Tables 60 (1995) 177.
[36] I. Angeli, INDC(HUN)-033 1999, private communication, 2003;
I. Angeli, Acta Phys. Hung. 69 (1991) 233.
[37] T. Suzuki, et al., Nucl. Phys. A 630 (1998) 661.
[38] E. Wesolowski, J. Phys. G: Nucl. Phys. 10 (1984) 321.
[39] M. Keim, et al., Nucl. Phys. A 586 (1995) 219.
[40] G.A. Lalazissis, M.M. Sharma, Nucl. Phys. A 586 (1995) 201.
[41] Isotope explorer, http://ie.lbl.gov/isoexpl/isoexpl.htm.
[42] B.V. Carlson, D. Hirata, Phys. Rev. C 62 (2000) 054310;
E. Baldini-Neto, B.V. Carlson, D. Hirata, in preparation.
[43] L. Chulkov, et al., Nucl. Phys. A 609 (1996) 74.